Geosciences Journal
Vol. 14, No. 3, p. 277 − 287, September 2010
DOI 10.1007/s12303-010-0028-y

A time-series SAR observation of surface deformation at the southern end of the San Andreas Fault Zone

Min-Jeong Jo, Joong-Sun Won*: *Department of Earth System Sciences, Yonsei University, Seoul 120-749, Republic of Korea*
Sang-Wan Kim: *Department of Geoinformation Engineering, Sejong University, Seoul 143-747, Republic of Korea*
Hyung-Sup Jung: *Department of Geoinformatics, The University of Seoul, Seoul 130-743, Republic of Korea*

ABSTRACT: The San Andreas Fault (SAF) is a continental transform fault that exists as a consequence of the relative motion of the Pacific and North American Plates. Differential SAR interferometry (DInSAR) particularly with a time-series analysis is an effective tool for long-term monitoring of the SAF. Radar interferometric phase, however, contains unwanted noises originated from atmosphere as well as observation system. For studying characteristics of interferometric phase at the southern end of the SAF zone, ERS–1/2 data, acquired from 1992 to 1999, and ENVISAT data, from 2003 to the present, were utilized. Troposphere interference and orbit error were the most significant sources of errors. Since the phase noise highly correlates with topographic elevation, a simulated interferogram from topographic elevation was utilized to compensate for the tropospheric signal delay. After subtracting the simulated phase from each DInSAR interferogram, more reliable results were obtained. These results are supported by comparison with the geodetic GPS data set.

Key words: InSAR, San Andreas Fault, tropospheric signal delay, time-series analysis, SBAS

1. INTRODUCTION

Earthquakes, volcanic activity, landslides, and other natural disasters frequently occur throughout the world. With each event, the possibility of enormous economic and human loss exists. For instance, the devastating earthquake that occurred along the Sichuan basin in China killed many and collapsed numerous buildings and bridges (Parsons et al., 2008). Repair work is still ongoing in New Orleans, which was attacked by Hurricane Katrina and underwent major flooding (Dixon et al., 2006). In order to minimize the damages from these natural disasters, it is necessary to build an effective and continuous monitoring system.

Differential synthetic aperture radar interferometry (DInSAR) is a promising technique that has been effectively used to observe surface deformations along the radar line-of-sight direction with an accuracy of a few millimeters (Massonnet and Feigl, 1998). DInSAR is a well-known technique that allows for the analysis of surface deformations in geologic phenomena, such as ground subsidence, earthquakes, and volcanic activities (Kim et al., 2008; Massonnet et al., 1993, 1995). While the DInSAR approach with one interferogram is only useful for the analysis of a single deformation episode, the interest of the scientific community is now moving towards the observation of temporal variations according to a series of SAR images. The small baseline subset (SBAS) algorithm, as a robust time-series analysis which only uses small baseline interferograms to suppress the spatial decorrelations, was proposed by Berardino et al. (2002).

The purpose of our study is to study the time-series surface deformations at the southern end of the San Andreas Fault (SAF) zone by using the SAR interferometry time-series analysis. Geologic estimates regarding the slip rate of the San Andreas Fault have been made in several ways (Bennett et al., 2004; Lundgren et al., 2009; Lyons and Sandwell, 2003). Estimation using the radar system was also successfully performed (Lyons and Sandwell, 2003; Fialko, 2006). High-resolution measurements of interseismic deformation across the southern San Andreas Fault system using space-borne SAR data were presented by Fialko (2006). It is reported that the inferred LOS velocity was 13–14 mm/yr during a time interval between 1992 and 2000.

From the previous studies, the atmospheric effects were revealed as a serious error source for the radar measurement in this area. Thus, adequate corrections for the tropospheric signal delay and for imprecise orbit information would make the estimates more reliable. The effect of water vapor on the SAR signal develops vertical stratification in the interferogram, and is only found on the places with topographic variation (Hanssen, 2001). This systematic error may prevent radar measurements from providing the actual surface deformations because the phase contribution of tropospheric delay is often much larger than geologic strains. Thus, in order to measure the subtle surface deformations effectively during the period of fault slip, it is necessary to alleviate the tropospheric delay. In this study, the SBAS method is applied to study the consistent surface deforma-

*Corresponding author: jswon@yonsei.ac.kr

tion at the southern end of the SAF zone. For the analysis, ERS–1/2 data, acquired from 1992 to 1999, and ENVISAT data, from 2003 to the present, were utilized to examine the temporal variations. The ERS data after the year 1999 was not used for this work because the Hector Mine earthquake was occurred on the upward part of northwest area in 16 October 1999. We could find the fact that interferograms which include the data after the earthquake were affected by that event.

Here we particularly focus on removal of atmospheric effects that often result in serious errors in this area. Considering the characteristics of the signal delay, suppression of tropospheric delay was carried out to refine the interferograms. It makes the result of the time-series analysis more reliable. The results are compared with the geodetic GPS data set for the verification.

2. STUDY AREA

The San Andreas Fault is a well-known continental transform fault that exists as a consequence of the relative motion of the Pacific and North American plates. The fault runs a length of approximately 1,100 km in California and runs northwest to southeast (Powell, 1992). It is commonly designated as the San Andreas Fault system due to the many branches that are stretched out in a sub-parallel direction of the main fault. Since a huge earthquake within the SAF zone has the potential to result in enormous economic and human losses, monitoring the behavior of the fault zone is necessary in order to better prepare for these risks and minimize damages.

One of major concerns for the SAF zone is to understand the variations of post- and inter-seismic stress with regard to both time and space. Since imposing a stress on the crust induces the deformation of the rock material, the crust at the boundaries of the lithospheric plates could be migrated by the stress. This stress is closely related to the earthquakes that frequently occur along the fault zone, and many questions remain regarding the characteristics of earthquake phenomena such as the recurrence cycle and rupture patterns (Smith and Sandwell, 2006). Therefore, the studies of geologic estimates regarding the slip rate of the fault zone have been carried out in several fields (Bennett et al., 2004; Lundgren et al., 2009; Lyons and Sandwell, 2003).

The study area is located in the southern end of the San Andreas Fault zone, across the Salton Sea region, which is defined as N32°30′–N34°30′ and W114°30′–W117°. It is well known from the geologic map that there are many fault traces, including active fault lines that exist in this region (Fig. 1). While most of the southern San Andreas Fault

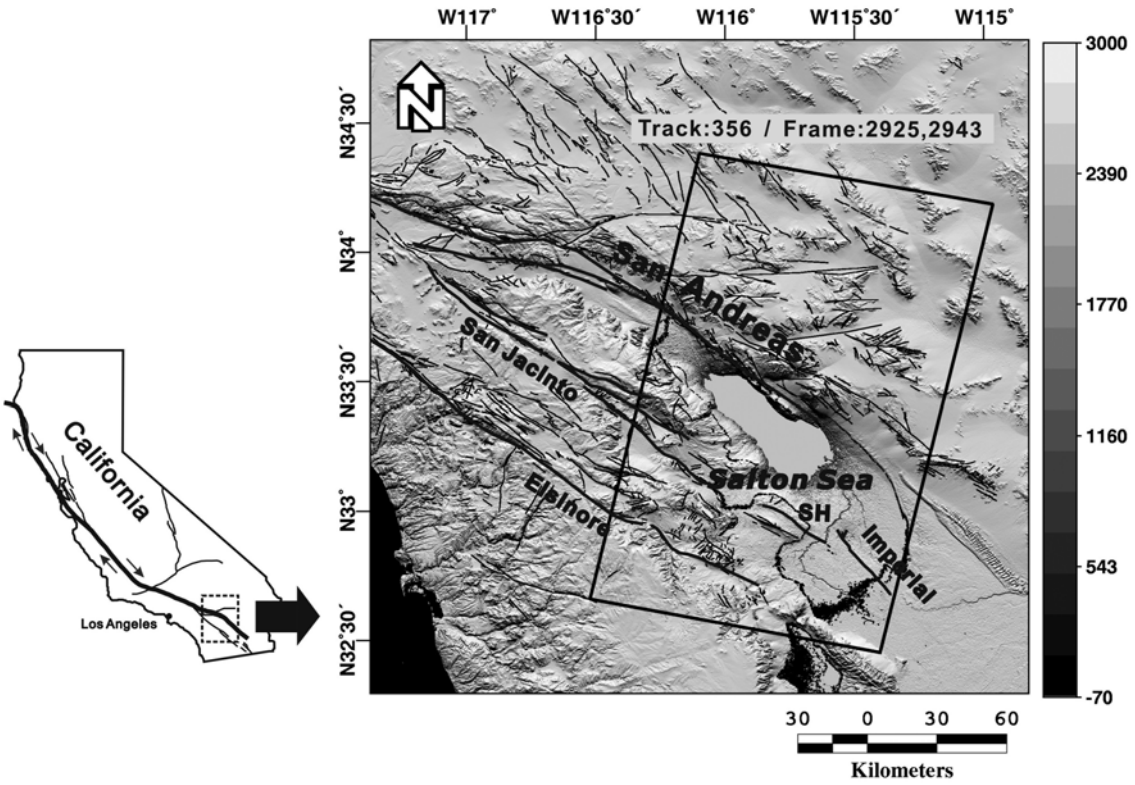

Fig. 1. Index map and shaded topographic relief map of the southern end of the San Andreas Fault, which includes the Quaternary and Holocene age fault. Thick lines represent the major active faults in this region. The rectangle outlines the InSAR track (356) and frames (2925, 2943) that were used in this study. The color legend shows the topographic height of this region using a meter scale (m). SH: Superstition hills fault.

zone is arid and dry, the agricultural areas located northeast and southwest of the Salton Sea induce significant decorrelation between the SAR images. Since the phase from the decorrelated area is noisy and unavailable for detecting small-scale deformations, we were only interested in the areas showing high coherence and long wavelength deformation. This fault zone has more than 2,500 meters of topographic relief (Lyons and Sandwell, 2003). To prevent spatial decorrelation and avoid a DEM error due to the high relief, an accurate estimation and removal of the topographic phase are both critical steps.

3. SAR DATA SET AND PROCESSING

Multiple SAR images were utilized for the analysis of time-series surface deformation at the study area. Forty four ERS–1 and ERS–2 SAR data sets, between December 1992 and October 1999, and twelve ENVISAT ASAR data sets, from February 2003 to August 2008, were obtained as raw signal data. The two sets of SAR data were acquired from the descending track 356, continuous frames 2925 and 2943.

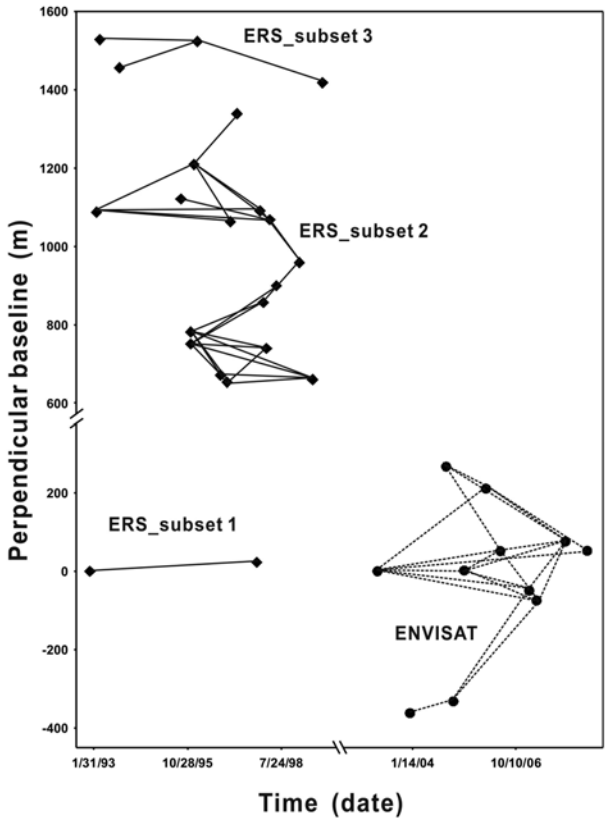

Fig. 2. The ERS–1/2 and ENVISAT ASAR image sets of the study area. The X-axis is the data acquisition time and Y-axis is the perpendicular baseline with respect to the reference image. Diamond shapes represent the ERS–1/2 SAR images, and circles represent the ENVISAT SAR data set. Thin solid and dashed lines indicate the interferogram pairs. ERS–1/2 interferograms are divided into three subsets.

We processed the raw signal data to single-look complex images using GAMMA Modular SAR Processor. Figure 2 lists the acquisition dates of the ERS–1/2 and ENVISAT SAR datasets and shows the relative perpendicular baseline with respect to the reference image, acquired the first date among each SAR dataset. The length of the perpendicular baseline was restricted to less than 150 meters for the ERS–1/2 interferogram pairs and to 300 meters for ENVISAT pairs, respectively. We obtained three small baseline subsets from the ERS dataset and only one subset from the ENVISAT dataset. A lack of ENVISAT data explains the higher limitation of the perpendicular baseline of the ENVISAT pairs. In this study, single-look complex images and interferograms were generated with the GAMMA Modular SAR Processor from Gamma Remote Sensing in Switzerland and the JPL/Caltech ROI_PAC software package.

Global Positioning System (GPS) survey data are required for the verification of InSAR measurements. Thousands of GPS stations are located throughout the San Andreas Fault zone to monitor the daily changes that occur. Time-series point geodetic datasets were obtained from the Scripps orbits and the Permanent Array Center (SOPAC), available at http://sopac.ucsd.edu/. Unfiltered raw signal data from five permanent GPS stations which includes north, east and up components of the station were used since the time span covers the entire period of the ENVISAT dataset. However, the daily time-series GPS data, including the time interval of the ERS–1/2, could not be obtained from the SOPAC site.

An interferogram of SAR data is constructed by measuring the phase difference between two single-look images. In an interferogram, the surface deformation is included, as are the phases of the topographic height, atmospheric, and thermal noise. The digital elevation model (DEM), via particularly the National Elevation Dataset (NED) with a resolution of 30 × 30 (m), was used to remove the topographic phase. Many of the interferograms generated from both the ERS–1/2 and the ENVISAT SAR data had tropospheric signal delay correlating with topographic elevation. The effect of these atmospheric constituents obscures the actual surface deformation. To minimize atmospheric effect, qualified components of the ERS–1/2 interferograms were used. The qualified interferograms are selected under the conditions of high coherence, short baseline and less interference from troposphere. Some interferograms showing severe spotted atmospheric effect are also extracted in the process.

However, selective use of the ENVISAT was not possible due to the lack of data. To remove the tropospheric delay, the simulated interferogram, whose phase correlates with the topographic elevation, was subtracted from each of the ENVISAT interferograms. After this tropospheric correction, calibrated and better results could be obtained.

In this study, the small baseline subset (SBAS) method was applied in the time-series analysis. When an interferogram is made using data paired with large perpendicular

baselines, it is difficult to match the SAR images. Even if the SAR images are co-registered, the baseline decorrelation increases due to less overlap of range bandwidth. As a consequence, errors in the interferogram increase due to the decorrelation between the SAR images. A key limitation of the SBAS method is that interferogram pairs that are used to analyze the time-series observation must be acquired from relatively close tracks in order to overcome spatial decorrelation (Berardino et al., 2002).

The phase in a topographically corrected interferogram can be expressed as follows:

$$\delta\phi_{A-B} = \delta\phi_{def} + \delta\phi_{atm} + \delta\phi_{orb} + \delta\phi_{topo} + \delta\phi_{noise},$$

where $\delta\phi_{A-B}$ is the phase difference between times A and B, $\delta\phi_{def}$ is the phase contribution due to surface deformation in the satellite line-of-sight (LOS) direction, $\delta\phi_{atm}$ is the phase contribution caused by atmospheric effects, $\delta\phi_{orb}$ is the phase due to inaccurate orbit, and $\delta\phi_{topo}$ is the residual topographic phase that is induced by the DEM error. The final variable, $\delta\phi_{noise}$, is the phase that is due to the mis-coregistration between the SAR images and thermal noise effects (Hooper et al., 2004). With the SBAS algorithm, it is possible to reduce the phase contributions that are induced by several error effects. To compensate for the atmospheric effect in the interferogram, spatially low-pass filtering and temporally high-pass filtering are adopted in order to consider the characteristics of atmosphere variation (Berardino et al., 2002).

For the enhanced results, we particularly applied the refined SBAS algorithm proposed by Jung et al. (2008). This algorithm also performs unwrapping error minimization and time-varying noise suppression. Detailed descriptions of the SBAS algorithm that was used in this study are provided by Berardino et al. (2002) and Jung et al. (2008).

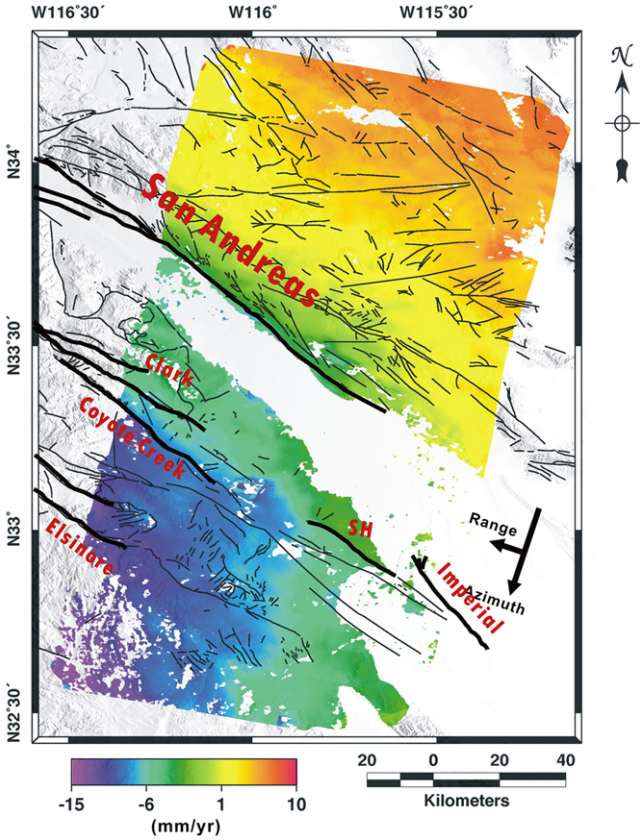

Fig. 3. LOS surface deformation rate map as estimated by the SBAS algorithm at the southern end of the San Andreas Fault zone from December 1992 to October 1999. Arrows indicate the flight (azimuth) and look (range) directions of the satellite. Thick lines represent well known active faults of this area. SH: Superstition Hills fault.

4. RESULTS

4.1. Analysis of ERS–1/2 SAR Data

To observe the temporal variation of the southern end of the SAF zone, we used 30 differential interferograms that were generated from the ERS–1 and ERS–2 single-look complex (SLC) images. Initially 141 interferograms were constructed from 18 SLC images, but many suffered severe atmospheric effects or spatial decorrelations and these were excluded from the time-series analysis. While the fairly arid areas of the SAF zone preserved high phase coherence throughout the period of observation, the steep or agricultural areas were decorrelated with noise and the unusable phase. After masking the low coherence areas based on the threshold value of 0.5, the DInSAR interferograms were unwrapped using the Minimum Cost Flow (MCF) algorithm (Costantini, 1998). Figure 3 shows a LOS surface deformation rate map estimated by the SBAS algorithm at the southern end of the San Andreas Fault zone from December 1992 to October 1999.

Although several interferograms show the phase contribution due to the inaccurate orbit, residual orbital correction was not conducted because we are interested in the observation of long-wavelength signal that is related to tectonic movement (Fialko, 2006; Lundgren et al., 2009). The noise component, specifically a residual orbit error, was assumed to be sufficiently mitigated according to an accumulation of the large volume of temporally uncorrelated images (Biggs et al., 2007). However, as shown in Figure 3, we were able to identify an apparent residual linear ramp from the northeast to the southwest corner in the negative direction. These linear terms were considered as the residual orbit error, and a similar phenomenon appeared in other studies as well. To overcome the inaccuracy of the orbit problem, a best-fit correction using GPS data or a de-trending correction of the InSAR data were carried out in other studies (Fialko, 2006; Lundgren et al., 2009). Therefore, additional correction using the GPS data was necessary to compare our results with those

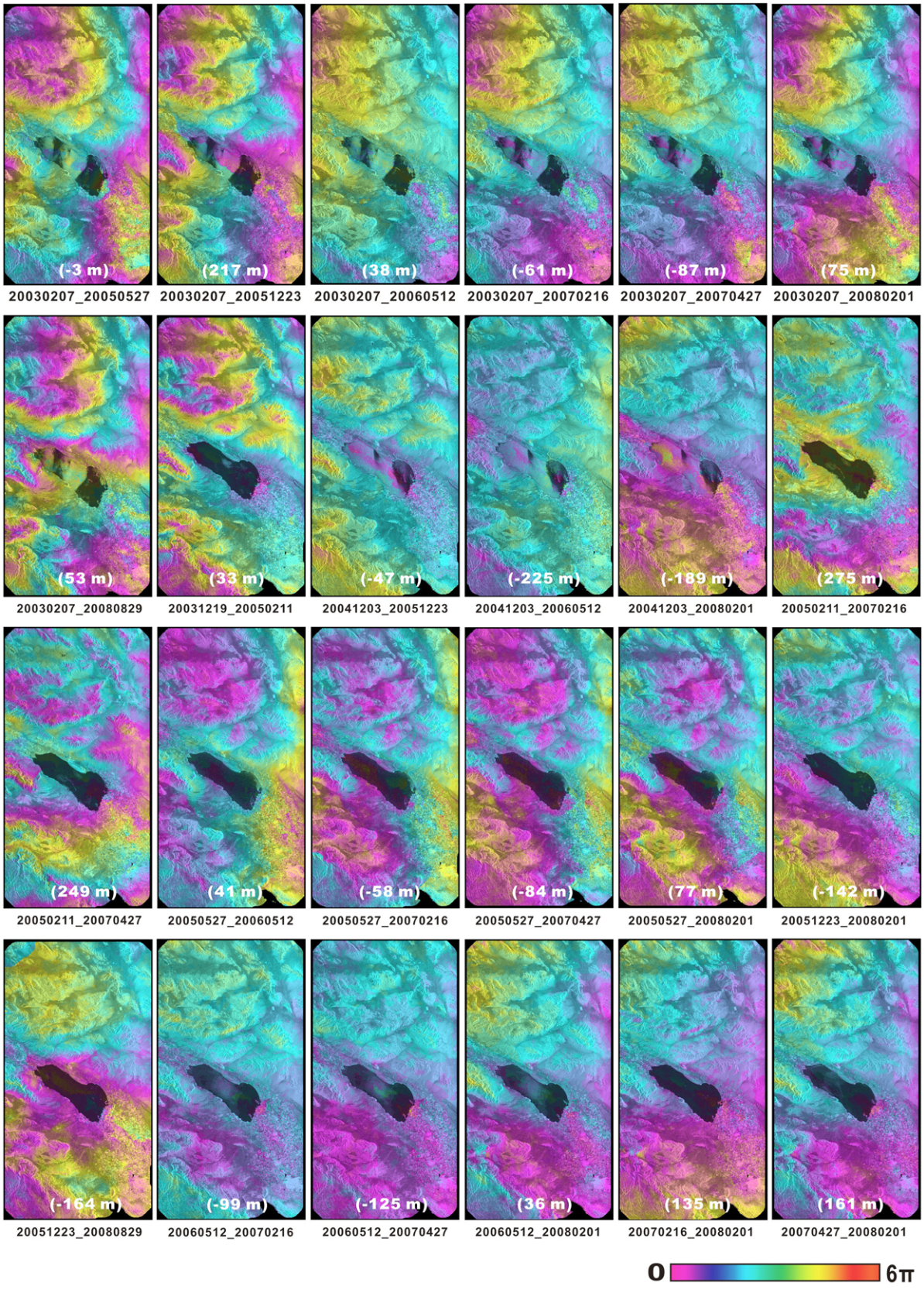

Fig. 4. Phase unwrapped DInSAR interferograms of ENVISAT data set from February 2003 to August 2008. The color scale represents the relative displacement in the line-of-sight direction. The values in the brackets denote the perpendicular baseline of each DInSAR interferogram. A color cycle is equal to 6 pi of phase variation.

of other studies.

Although precise estimates could not be obtained from the ERS dataset due to the residual orbit error, the patterns of the surface motion were identifiable from the deformation rate map. The southern areas of the Salton Sea have many active faults which are sub-parallel with the main strike of the SAF zone, and they tend to move more rapidly toward the northwest than in the northern areas relatively. From this difference in velocities, it confirmed that the study area has a right-lateral (dextral) motion along the SAF.

4.2. Analysis of ENVISAT SAR Data

4.2.1. Atmospheric correction of the DInSAR interferogam

For the ENVISAT ASAR data set, 24 DInSAR interferograms were constructed from 11 single look complex images (Fig. 4). To accommodate the insufficient amount of ENVISAT SLC data the interferometric pair with perpendicular baseline less than 300 meters was selected. As a result, only one baseline subset was obtained for the SBAS processing (Fig. 2). A good interferogram with a 5-year time interval was also generated since the study area preserved high phase coherence regardless of the temporal variation.

Some of the DInSAR interferograms, such as [20030207_20070427], properly showed the expected surface deformation of the southern end of the SAF zone. The northern areas of the Salton Sea are relatively stable, whereas the southern areas show large movement towards the northwest direction. However, several of the interferograms show atmospheric effects, specifically tropospheric signal delay, as shown in Figure 4. The interferograms [20030207_20051223], [20031219_20050211], and [20050211_20070427] clearly show the phase contribution as a result of these tropospheric effects. In the northern areas of the Salton Sea, the phase patterns correlate with the topographic elevation. To better understand the correlation between the phase and topographic elevation, correlation analysis was carried out for some of the interferograms (see Fig. 5). All pixel values in an interferogram were plotted for the northern parts of the study area. The interferograms [20030207_20051223] and [20050211_20070216] showed the highest correlation coefficient among the analyzed interferograms of 0.93 and 0.85, respectively. As shown in Figure 5, the data clouds represent linear relationships in the negative and positive direction, depending on the change of atmospheric condition at the data acquisition time. Since the phase contributions due to tropospheric effects are much larger than the actual surface deformations, these delayed components need to be separated from the interferogram.

Non-corrected DInSAR interferograms contain the phase contribution induced by an inaccurate orbital in addition to the atmospheric effect. While the residual orbit correction was not applied to the ERS–1/2 data to prevent a loss of long-wavelength component presumably related with deformation signal, it is difficult to sufficiently mitigate the residual orbit errors in the SBAS processing due to the lack of ENVISAT images. In fact, a specific directional linear ramp was observed when the interferograms were used including

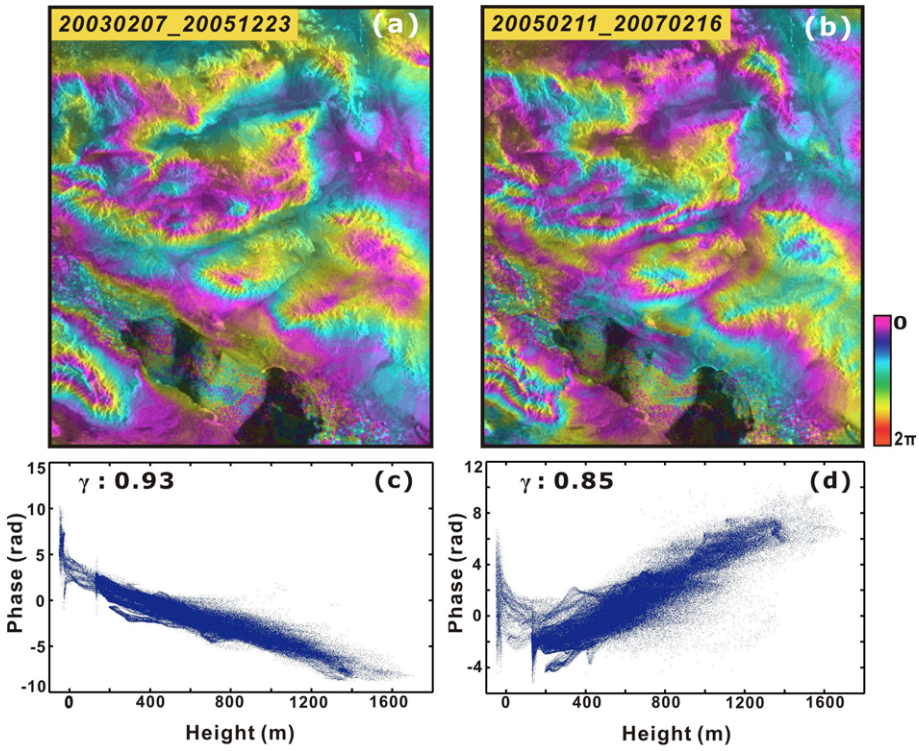

Fig. 5. The tropospheric signal delay on the interferogram, 20030207_20051223, which correlates with a topographic elevation (a), (b) and the interferograms show an opposite direction of the fringe pattern, which depends on the role of the troposphere delayed image. The plotted graphs (c) and (d) denote the correlation coefficient between the height and phase at the study area for the interferograms (a) and (b), respectively. γ indicates a correlation coefficient.

those with non-corrected orbit information.

To remove unwanted phases by both tropospheric delay and orbit error, we applied the new algorithm as followed. The orbit error, $\delta\phi_{orb}$, was modeled by tilting plane and tropospheric delay, $\delta\phi_{atm}$, was modeled by a third-order equation as follows:

$$\delta\phi_{orb} = b_1 x + b_2 y + c_1 ,$$
$$\delta\phi_{atm}^{topo} = a_1 z^3 + a_2 z^2 + a_3 z + c_2 ,$$

where (x,y) is a range and azimuth coordinate and z is a topographic height. The parameter of b_1, b_2, a_1, a_2, a_3, and c ($= c_1 + c_2$) from each interferogram can be estimated by:

$$\begin{bmatrix} x_1 & y_1 & z_1^3 & z_1^2 & z_1 & 1 \\ x_2 & y_2 & z_2^3 & z_2^2 & z_2 & 1 \\ & & \vdots & & & \\ & & \vdots & & & \\ x_n & y_n & z_n^3 & z_n^2 & z_n & 1 \end{bmatrix} \begin{bmatrix} b_1 \\ b_2 \\ a_1 \\ a_2 \\ a_3 \\ c \end{bmatrix} = [\phi_{orb} + \delta\phi_{atm}^{topo}] .$$

The simulated interferogram whose phase correlates with topographic elevation was generated from a_1, a_2, a_3, and c, and subtracted from each DInSAR interferogram. After removing tropospheric delay, only the range directional linear ramp was corrected during baseline optimization in order to mitigate orbit error, based on the assumption that the surface deformation due to the tectonic motion would show a gradual change in azimuth direction (Fialko, 2006; Lundgren et al., 2009).

Figures 6a and b show the example interferograms before and after the correction, respectively. Most residual phases related with topography and orbit error were removed by the corrections. The boxed zone in Figures 6a and b outlines the area used for the analysis. Figure 6c shows the variations of relative LOS displacements extracted from the interferograms at each processing level in order to examine which anomalous component is the most contributive. The phases in the interferograms were first converted into the line-of-sight displacement, and then averaged values in both range and azimuth directions were extracted as shown in Figure 6c. The empty triangles represent the relative displacement in the non-corrected interferogram, showing a linearly increasing pattern with significant fluctuations. Since the non-corrected interferogram contains the phase contribution due to the tropospheric signal delay, this fluctuation correlates with the topographic elevation. The overall growth pattern is induced by the residual orbit errors. From the distribution marked with stars after the orbit correction, this linear ramp, positive growth pattern shown on the initial interferogram, was no longer appeared. However, the distribution still shows considerable fluctuation that is also closely related with the topographic height variation. This noise might surpass the actual surface deformations by the tectonic motion. From the distribution with filled triangles, after residual orbit and tropospheric delay corrections, the fluctuation in large-scale did not appear anymore. Locally fluctuated shapes, however, remain on the A'-side (Fig. 6c). It is presumed that inaccurate tropospheric effect modeling induced the residual errors. These small-scale errors could be corrected in further time-series analysis. The relative

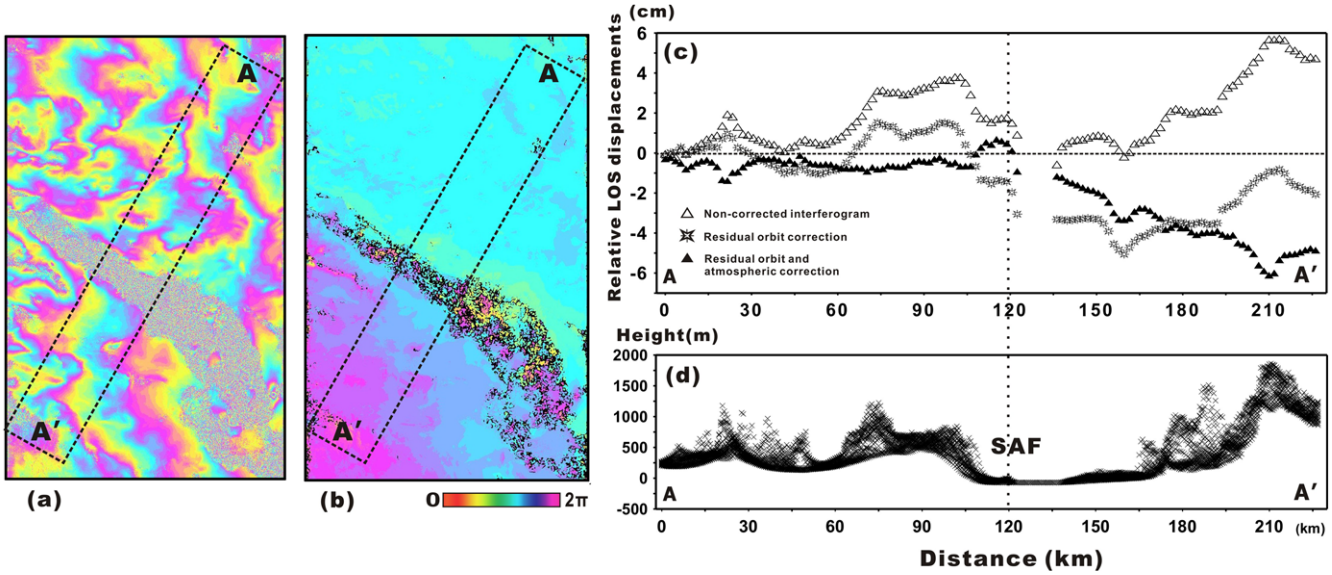

Fig. 6. The example of tropospheric phase correction of the 20030207_20051223 pair. (a) initial (uncorrected) interferogram, (b) interferogram after residual orbit and tropospheric phase correction. Black dotted box in (a) and (b) outlines a profile (A–A′) in (c). (c) LOS displacements along the profile of A–A′ depending on the correction levels: Empty triangles, stars, and filled triangles indicate the values on non-corrected interferogram, residual orbit corrected interferogram, and orbit and atmospheric corrected interferogram, respectively. (d) The topographic heights of the study area along the profile.

deformations in the fully corrected interferogram are very small at the north to the San Andreas Fault. South to the fault, however, a steep slope in negative direction is observed as displayed by filled triangles in Figure 6c. This linear pattern agrees well with the previous studies that deformation rates of the northern parts didn't show a noticeable variation and southern parts showed a gradual change (Fialko, 2006; Lundgren et al., 2009). The amount of migration grows with the distance from the San Andreas Fault. These results demonstrate that atmospheric correction particularly for the tropospheric delay is an effective and mandatory process in the study area and the fully corrected interferogram is very useful to study the crustal deformation pattern.

4.2.2. Time-series analysis using SBAS method

After masking the pixels in the low coherence regions (lower than 0.7), all of the DInSAR interferograms were unwrapped using the MCF algorithm as with the ERS dataset.

Figure 7 shows the LOS deformation velocity map generated from uncorrected ENVISAT interferogrmas. The main difference between the two velocity maps generated from uncorrected and tropospheric corrected interferograms is the deformation rates at the southern parts of the fault. As shown on the graphs in Figure 7, InSAR measurements are practically not matched to the GPS data. Quite a number of InSAR measurements are underestimated than GPS values, and also show some fluctuations. As a result of this distribution of InSAR measurements, deformation rates of the southern parts of the fault are underestimated. It is presumed that these errors are induced by the tropospheric effect. Locally varying patterns over the study area are also shown on the velocity map. Therefore, it is inappropriate for the analysis of time-series surface deformation of the fault zone. It is the reason why corrected interferograms should be used for the analysis.

Figure 8 displays the satellite line-of-sight velocity map generated from corrected ENVISAT interferograms. The local patterns which are presumed as errors are no longer observed on the map.

A prominent asymmetry of the deformation rate is recognized between the southern and northern areas of the Salton Sea. The deformation rate of the northern areas are

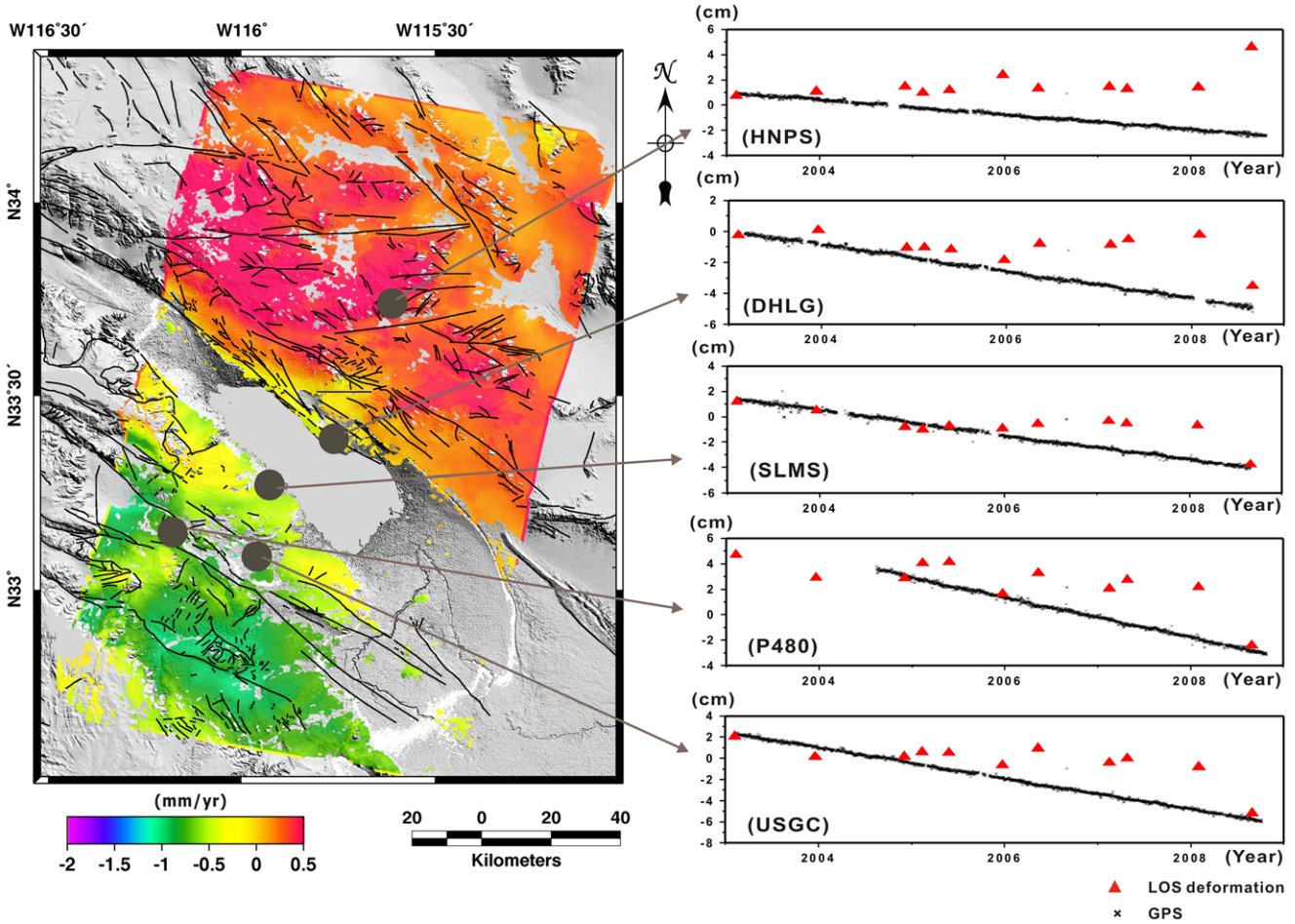

Fig. 7. The LOS (line-of-sight) surface velocity map generated from uncorrected ENVISAT DInSAR interferograms from February 2003 to August 2008. The graphs show the comparisons between the GPS and the time-series InSAR measurements. Tiny black dots are the daily GPS data and the red triangles are the measured InSAR deformations. Uncolored areas represent a low coherence region.

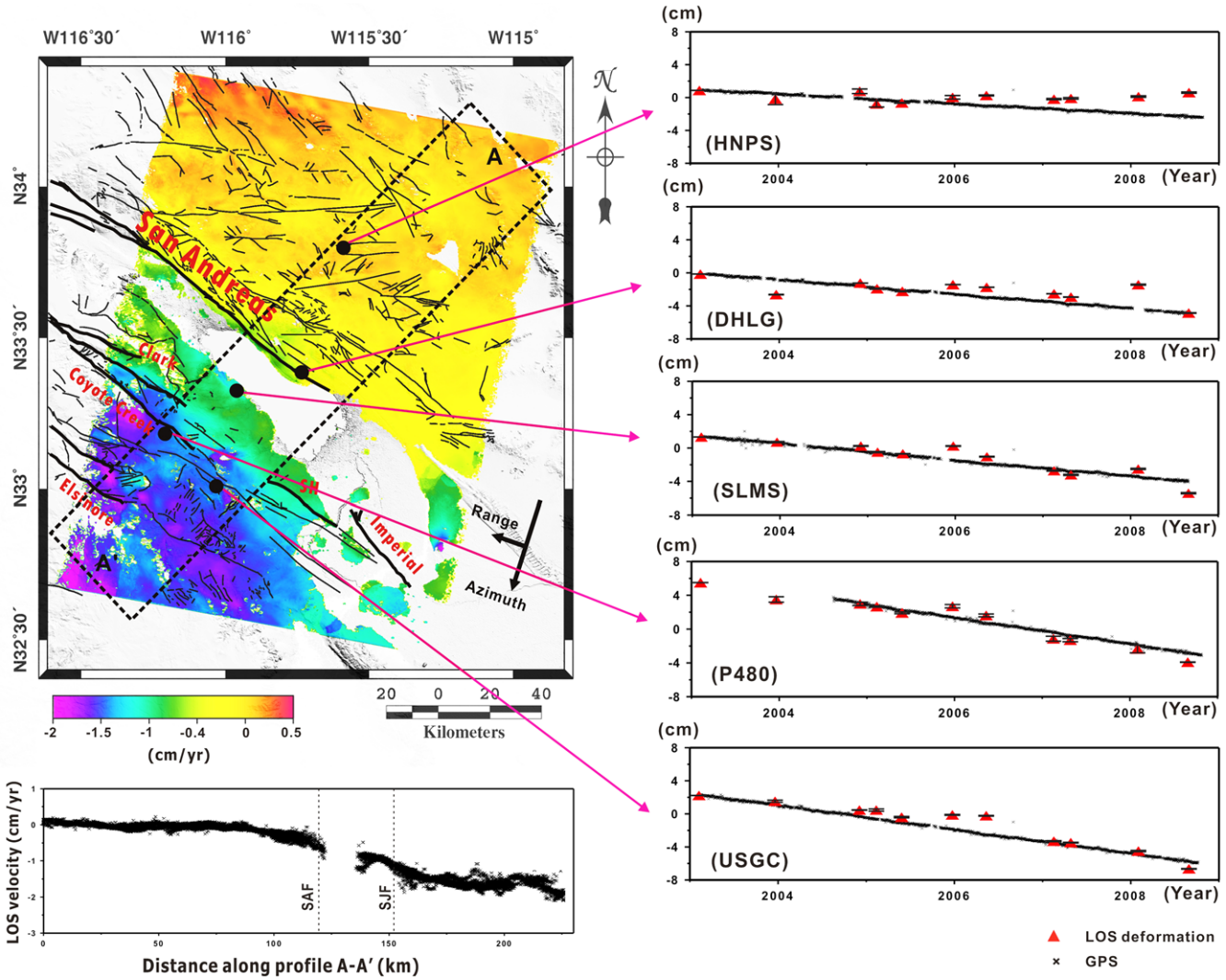

Fig. 8. The LOS surface velocity map generated from the ENVISAT DInSAR interferograms after tropospheric delay correction from February 2003 to August 2008. The black box outlines a profile (A–A′) of the measurements extracted from the velocity map. Vertical dashed lines in the cross section denote position of the mapped SAF trace and the assumed SJF position. The graphs show the comparisons between the GPS and the time-series InSAR measurements. The indexes of the symbols are the same in Figure 7.

relatively constant, but the southern areas show a gradual change as far away from the geologic fault trace of the SAF. This finding is ensured with the profile A–A′ that is shown in the velocity map. Adjacent to the position of the mapped SAF trace, the line-of-sight velocity maintains a nearly stationary rate, but a steep slope begins near the position of the fault trace. The estimated LOS velocity of the SAF is 17–18 mm/yr and the maximum velocity that was measured from the southern areas is –24 ± 6.5 mm/yr. Assuming that this signal was purely obtained from the surface displacement and that the SAF predominantly moves along the local strike of the SAF, then the estimated LOS velocity corresponds to a horizontal velocity of ~50 mm/yr (Lyons and Sandwell, 2003). This estimate is somewhat higher than other estimates, which were inferred from a different period that was based on radar observation or using a geologic method (Fialko, 2006; Bennett et al., 2004).

To validate the results of this study, comparisons between the time-series GPS and InSAR measurements were also performed using the five permanent station data sets (Fig. 8). The GPS data was projected in the radar line-of-sight direction in order to match the coordinates to one another. Only the horizontal components of the GPS measurements were used to make reliable comparisons because the vertical components have large fluctuations with low accuracy. Mean standard deviation of the daily GPS data estimated by using horizontal components is about 0.11 cm. The comparison is more stringent when using the unfiltered GPS data. The comparison with three stations especially at the southern areas apparently shows good agreement. The difference between the velocities measured using the InSAR and GPS data is less than ±0.1 cm/yr at the SLMS, P480, and USGC

Table 1. The comparison of surface deformation velocity between the InSAR and GPS data set

(Units: cm/year)

GPS station ID	LOS velocity by GPS	LOS velocity by InSAR
HNPS	–0.59	0.012
DHLG	–0.87	–0.44
SLMS	–0.98	–1.09
P480	–1.57	–1.62
USGC	–1.46	–1.55

sites. These estimates also support that the southern areas of the SAF has more active motion than the northern areas. The LOS surface velocities that were estimated from both the InSAR and GPS time-series data are summarized in Table 1. As shown in the graphs, some differences between the two data sets are presented on the HNPS and DHLG stations. It is likely that the misfit on the DHLG site was caused by an unwrapping error. The disagreement on the HNPS site may be due to the phase contribution of the way the atmosphere randomly appeared. To compensate for this atmospheric effect in the interferogram, spatially low pass filtering and temporally high pass filtering was adopted when considering the characteristics of atmosphere variation (Berardino et al., 2002). However, it is difficult to completely remove these phase components. An alternative possibility to explain the disagreements with the HNPS site is that unreliable measurements were obtained as a consequence of the inaccurate estimation of the simulated interferogram.

5. CONCLUSIONS AND DISCUSSION

We explored the temporal variations of surface at the southern end of the San Andreas Fault zone particularly the areas around the Salton Sea region using a time-series analysis of SAR data. The inferred results demonstrate that the SAR observation system is a robust and effective technique for observing surface deformation. The SBAS method as time-series analysis also contributes to the compensation of errors that are induced by the imprecise topographic and orbit information and the atmospheric effect that are randomly appeared in time. However, the tropospheric signal delay that is shown on some of the interferograms was not mitigated through the SBAS method. In our study, subtracting the simulated phase that correlates with the topographic elevation was adopted. After subtracting the simulated phase from each DInSAR interferogram, more reliable results were obtained with the maximum velocity of –24 ± 6.5 mm/yr at the southern areas of the Salton Sea. These results are supported by comparison with the geodetic GPS data set. The asymmetry of the deformation rate at the southern end of the SAF zone was recognized with both the analyses of the ERS and ENVISAT data. Over the northern parts of the fault showed constant deformation rates, but the southern parts showed a gradual change as far away from the geologic fault trace of the SAF. The dextral strike-slip motion of the fault zone is confirmed from the difference between velocities across the fault. While the corrected interferogram made the results more reliable based upon the comparison with geodetic data, the problem of the lack of input data still remains. Ideally, having and using more data would yield better results.

The discrimination between the vertical and horizontal components is also meaningful in regards to the SAF zone. For this work, the results obtained from different geometric positions based upon the radar system were required. Unfortunately, it is difficult to observe the LOS deformation using the ascending data since the flight direction of the satellite is sub-parallel to the main strike of the fault zone. Another problem with the ascending data is the severe tropospheric effect. Since the ascending data includes more regions with high relief, it results in estimates that are unusable. Despite these difficulties, the potential for observing distinguishable deformation from the noise still remains when using long-term period interferograms.

ACKNOWLEDGMENTS: This work was supported by the Korea Research Foundation Grant (KRF–2009–013–C00051). This study has also been carried out under the Nuclear R&D Program [No. 2010–0001070] supported by the Ministry of Education, Science and Technology, Republic of Korea.

REFERENCES

Bennett, R.A., Friedrich, A.M., and Furlong, K.P., 2004, Codependent histories of the San Andreas and San Jacinto fault zones from inversion of fault displacement rates. Geology, 32, 961–964.

Berardino, P., Fornaro, G., Lanari, R., and Sansosti, E., 2002, A new algorithm for surface deformation monitoring based on small baseline differential SAR interferograms. IEEE Transactions on Geoscience and Remote Sensing, 40, 2376–2383.

Biggs, J., Wright, T., Ju, Z., and Parsons, B., 2007, Multi-interferogram method for measuring interseismic deformation: Denali Fault, Alaska. Geophysical Journal International, 170, 1165–1179.

Costantini, M., 1998, A novel phase unwrapping method based on network programming. IEEE Transactions on Geoscience and Remote Sensing, 36, 813–821.

Dixon, T.H., Amelung, F., Ferretti, A., Novali, F., Rocca, F., Dokka, R., Sella, G., Kim, S.W., Wdowinski, S., and Whitman, D., 2006, Subsidence and flooding in New Orleans. Nature, 441, 587–588.

Fialko, Y., 2006, Interseismic strain accumulation and the earthquake potential on southern San Andreas fault system. Nature, 441, 968–971.

Hanssen, R.F., 2001, Radar Interferometry: Data Interpretation and Error Analysis. Kluwer Academic Publishers, Dordrecht, 308 p.

Hooper, A., Zebker, H., Segall, P., and Kampes, B., 2004, A new method for measuring deformation on volcanoes and other natural terrains using InSAR persistent scatterers. Geophysical Research letters, 31(L2), 3611, doi:10.1029/2004GL021737.

Jung, H.S., Lee, C.W., Park, J.W., Kim, K.D., and Won, J.S., 2008, Improvement of small baseline subset (SBAS) algorithm for

measuring time-series surface deformations from differential SAR interferograms. Korean Journal of Remote Sensing, 24, 165–177. (in Korean with English abstract)

Kim, S.W., Wdowinski, S., Dixon, T.H., Amelung, F., Won, J.S., and Kim, J.W., 2008, InSAR-based mapping of surface subsidence in Mokpo City, Korea, using JERS-1 and ENVISAT SAR data. Earth Planets Space, 60, 453–461.

Lundgren, P., Hetland, E.A., Liu, Z., and Fielding, E.J., 2009, Southern San Andreas-San Jacinto fault system slip rates estimated from earthquake cycle models constrained by GPS and interferometric synthetic aperture radar observations. Journal of Geophysical Research, 114(B0), 2403, doi:10.1029/2008JB005996.

Lyons, S. and Sandwell, D., 2003, Fault creep along the southern San Andreas from interferometric synthetic aperture radar, permanent scatterers, and stacking. Journal of Geophysical Research, 108(B1), 2047, doi:10.1029/2002JB001831.

Massonnet, D., Rossi, M., Carmona, C., Adragna, F., Peltzer, G., Fiegl, K., and Rabaute, T., 1993, The displacement field of the Landers earthquake mapped by radar interferometry. Nature, 364, 138–142.

Massonnet, D., Briole, P., and Arnaud, A., 1995, Deflation of Mount Etna monitored by spaceborne radar interferometry. Nature, 375, 567–570.

Massonnet, D. and Feigl, K.L., 1998, Radar interferometry and its application to changes in the earth's surface. Review of Geophysics, 36, 441–500.

Parsons, T., Ji, C., and Kirby, E., 2008, Stress changes from the 2008 Wenchuan earthquake and increased hazard in the Sichuan basin. Nature, 454, 509–510.

Powell, R.E. and Weldon, R.J., 1992, Evolution of the San Andreas fault. Annual Review of Earth and Planetary Sciences, 20, 431–468.

Smith, B.R. and Sandwell, D.T., 2006, A model of the earthquake cycle along the San Andreas Fault System for the past 1000 years. Journal of Geophysical Research, 111(B0), 1405, doi:10.1029/2005JB003703.

Manuscript received February 10, 2010
Manuscript accepted August 24, 2010